STScI | SPACE TELESCOPE SCIENCE INSTITUTE

Instrument Science Report (STIS) 2022-01(v1)

Long-Term Rotational Evolution of the STIS CCD Flatfields

K. Ward-Duong[1,2], S. Lockwood[1], J. Debes[1], R. J. De Rosa[3]

[1] Space Telescope Science Institute, Baltimore, MD
[2] Smith College, Northampton, MA
[3]European Southern Observatory, Santiago, Chile

18 March 2022

ABSTRACT

We confirm a long-term rotational drift of 0.0031 degrees/year of the STIS CCD based upon analysis of 50CCD flatfields spanning over 20 years of calibration data. Using the dust motes present in the flatfields, we extract the positions of the motes in each image, allowing us to develop a catalog of stable, high 'signal-to-noise' mote features and track their relative positions over time. We find that the motes appear to be moving at the aforementioned rate relative to an approximate center of rotation located at X=468.02, Y=411.18 in detector pixel coordinates. Given the relatively large errors in centroiding the unusually-shaped and often asymmetric motes, we perform an MCMC slope-fitting analysis to derive an uncertainty on the rotation of $\pm$0.0001 degrees/year. Our derived rotation rate value is similar to two previous complementary CCD analyses: a measurement of spectral trace rotation in the grating L modes, and a time-dependent offset in detector true north position angle relative to the FITS header orientation keyword in science images. We therefore recommend that archival and future STIS CCD images should have their header information updated accordingly to account for this rotational drift. We also suggest similar corrections for rotational effects with respect to the reference files for spectral traces.

Operated by the Association of Universities for Research in Astronomy, Inc., for the National Aeronautics and Space Administration.

Contents

1. Introduction

The Space Telescope Imaging Spectrograph (STIS) on the Hubble Space Telescope (*HST*) features a wide range of both optical and ultraviolet (UV) imaging and spectroscopic capabilities. While STIS UV observations use multi-anode microchannel array (MAMA) detectors to cover the near-UV and far-UV, optical imaging and spectroscopy with STIS utilize a single charge-coupled device (CCD), which is the focus of this report. Previous analyses of the CCD have exhibited two time-dependent effects suggesting a possible rotational drift of the instrument: **(1)** variation between the tilt of the spectral traces derived from reference files and the tilt of spectra in science observations (Dressel et al., 2007, ISR 2007-03), and **(2)** astrometric analyses of archival imaging using sources in *Gaia* DR2 by Nguyen et al. (2021). The *Gaia* astrometric analysis provided evidence for a growing offset of the detector true north

angle from the telescope ORIENTAT header keyword, which measures the position angle of the image *y*-axis in degrees east of north. This growing offset was found to be unique to STIS, as it was not detected when Nguyen et al. (2021) applied similar analysis to *HST* Wide Field Camera 3 (WFC3) or Advanced Camera for Surveys (ACS) archival imaging.

The evidence for slowly-varying, long-term rotational effects in the STIS CCD has now been substantiated from distinct analyses using both STIS imaging and spectroscopic modes. The first of these analyses involved a study of the spectral trace rotation by Dressel et al. (2007), which demonstrated a rotational drift in the L mode grating traces of approximately 0.003 degrees/year. The separate analysis from the recently-published STIS imaging astrometric study by Nguyen et al. (2021) showed a slow drift in the true north angle of the STIS detector relative to its estimated telescope header north angle orientation at an estimated rate of 0.0038 degrees/year (Figure 1).

In this report, we describe a complementary and independent study to search for rotational variation by measuring the STIS CCD flatfields. This allowed us to determine whether a similar rotation effect was detected within purely instrument-internal images. Here, we demonstrate consistent results with the previous two studies and show that the rotational drift appears to be a physical effect intrinsic to the CCD itself. In Section 2, we describe the approach, which used positions of dust motes as a function of time to detect rotation in the CCD flatfields. In Section 3, we provide the results from identifying a stable set of motes and tracking their positions over a 20-year time baseline, and fit the observed trend to determine the rate of rotation of the CCD. Finally, in Section 4, we summarize the findings from this experiment and offer potential suggestions for correcting STIS CCD observations to compensate for the observed effect.

1.1 Studies of the spectral trace rotation

Long-term drifts in the rotation angle of the extracted spectral trace for various CCD spectroscopic modes (G230LB, G430L, G750L) was noted by Dressel et al. (2007) in a previous STIS Instrument Status Report (ISR 2007-03). Their measurements of seven years' of spectral trace extractions taken prior to Servicing Mission 4 (SM4, in 2009) showed a rotational drift of 0.003-0.004 degrees/year for the CCD L modes, highlighting the need for updated calibration files relative to the original trace position derived from standard reference files. Studies of the individual gratings resulted in rotation measurements in degrees/year of 0.0031 ± 0.0003 for G230LB, 0.0041 ± 0.0001 for G430L, and 0.0037 ± 0.0003 for G750L (noting that rotation rates for G230LB and G430L differ at the 3σ level).

Ongoing efforts within the STIS team to extend the spectral trace rotation by an additional decade and to characterize this effect for additional CCD spectroscopic modes have preliminarily shown that the rotation has remained similar for CCD spectral traces over the longer post-SM4 baseline of observations. Similar analyses for the MAMA spectral traces show that they do not rotate as much or show a similar trend

(Jones et al., in prep.). This extended analysis suggests that the spectral trace rotation is an effect limited to the CCD and is not endemic to the STIS instrument as a whole.

1.2 Motivation from Gaia astrometric analysis

To precisely measure the orbital properties of a companion orbiting a stellar debris disk system, Nguyen et al. (2021) performed a joint astrometric analysis of archival ACS, WFC3, and STIS imaging, spanning 14 years of observations. In order to derive precise astrometric solutions for each instrument, they queried *Gaia* DR2 to find all background stellar sources in proximity to their target star. They then extracted the positions of those stars in the *HST* images (for which ACS had two to three suitable sources, STIS had 15-20, and WFC3 had five to seven) and cross-matched them to the *Gaia* solutions. As part of this analysis, the authors discovered a systematic error affecting only the STIS images, which showed a significant offset in the derived true north angle of the detector relative to the orientation of the telescope as defined by the FITS header ORIENTAT keyword.

To further investigate the STIS offset, Nguyen et al. (2021) performed a much larger archival analysis of over 1000 reduced images from each instrument over a time baseline of 20 years, and cross-matched them with *Gaia* sources in each field to derive plate scale and orientation for each image. For the given epoch of images in 2017 investigated in their study, they found an average offset of 0.077 ± 0.002 deg between the true north angle of the detector and the header keyword value. The results of this investigation for the detector position angle of each instrument are visualized in Figure 1, showing the relative consistency over time for ACS and WFC3 and the steadily increasing offset for STIS (including both 50CCD and 50CORON observations). Fitting a slope to this drift shows a rotation rate of 0.0038 degrees/year, comparable with the slope of the spectral trace rotations derived by Dressel et al. (2007) from the L mode gratings.

1.3 Need for precision astrometry

The fidelity of the north angle measurement has important ramifications for any astrometric solution derived from STIS CCD imaging. It holds particular importance for the coronagraphic modes, wherein precision astrometry to within fractions of pixels is necessary to measure the orbits of stellar and planetary companions, to ascertain the positions or motion of circumstellar disks and their features, to explore temporal variation in resolved jet features/motion for protostars, and other scientific cases. As such, a careful assessment of the rotational behavior of the CCD and its time-dependence is requisite to correcting the position angle information in both archival and future observations in order to perform precision astrometry.

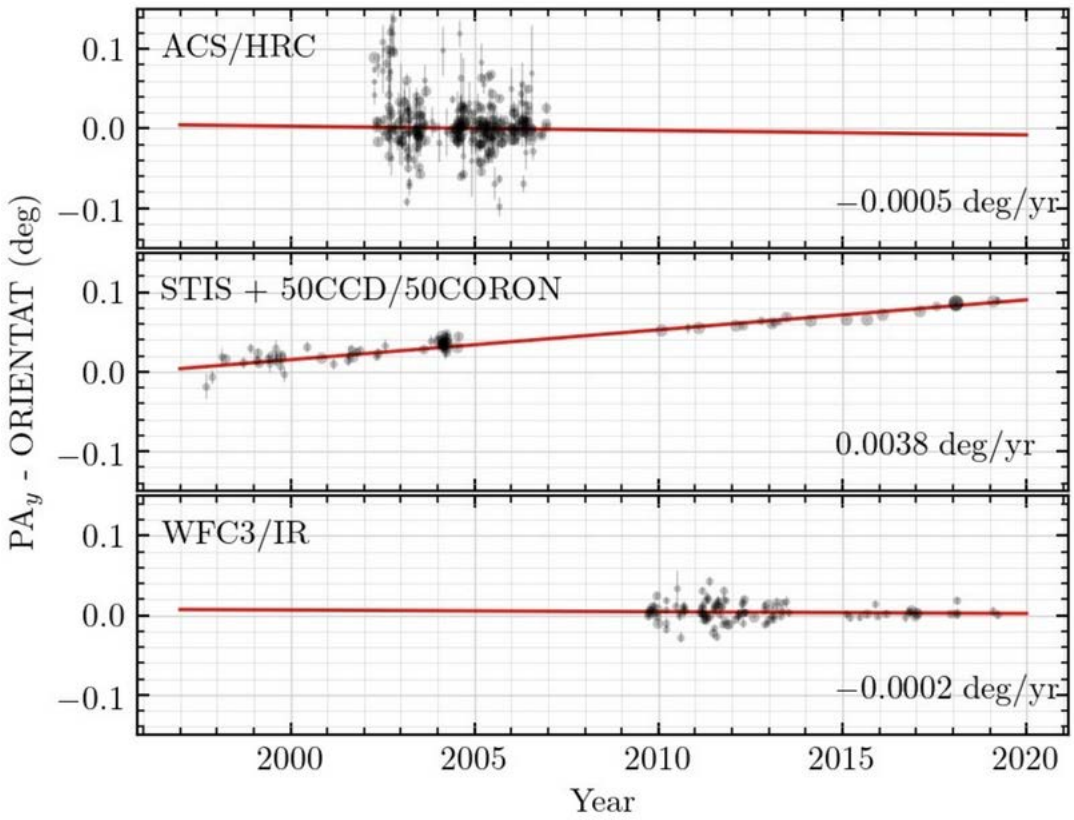

Figure 1. Offsets between the true north angle of the images (PA_y) and the telescope header orientation (ORIENTAT) for ACS, STIS, and WFC3, derived from cross-matching *Gaia* DR2 sources within *HST* archival imaging and measuring the position angle. Figure is based upon the analysis presented in Appendix B of Nguyen et al. (2021). While the offset measurement shows a long-term secular increase for STIS, it does not seem to vary significantly for imaging performed with either ACS or WFC3.

2. Methods

2.1 Dust mote extraction

To conduct the dust mote identification and analysis, all existing archival STIS 50CCD flatfields taken from Cycle 8 through Cycle 28 were downloaded (*flt.fits files). 50CORON flatfields were also downloaded and measured, but for simplicity (avoiding the coronagraphic bars and wedges, as shown in Figure 2) and in order to reliably identify the same catalog of dust motes across all epochs, these data were not combined with the 50CCD flats nor used in the main analysis in this report.

2.1.1 Flatfield processing

Each flatfield image was first inverted by taking the median of the flatfield, multiplying all pixel values by -1, and adding 2× the median value to all pixels in the image in order to avoid any negative pixel values. This approach was adopted for both the regular 50CCD flatfields as well as the 50CORON coronagraphic flats. Due to vignetting effects on the field corners (see Figures 2 and 3 for an example), the images were trimmed by 200 pixels in each axis, leaving a usable region of the flatfield that was more uniformly illuminated in an 800x800 pixel range.

2.1.2 Source finding algorithms

Two main source-finding algorithms in Astropy (Astropy Collaboration et al., 2018) were used to detect dust motes in the inverted flatfields. The first approach used the DAOStarFinder algorithm in *photutils*, as it provided the possibility to mask portions of the image directly, thereby avoiding spurious source edge effects or detections introduced by the sharp edges of the 50CORON coronagraphic aperture. Figure 3 shows the result of detecting sources in two epochs of 50CORON flatfields and comparing two sets of dust mote positions across each extraction.

The second approach utilized the *detectsources* module in *photutils*, which applies a watershed algorithm to the entire image in order to detect contiguous sources above a particular noise threshold. While the *detectsources* approach more reliably recovered faint motes seen in a visual inspection, the algorithm's inability to mask portions of the image proved challenging for the coronagraphic flatfields. As such, the subsequent analysis presented in this report focuses specifically on the 50CCD flatfields (noting that preliminary analyses of the 50CORON measurements show similar time-dependent rotational effects with slightly larger uncertainties than the results presented here).

The source detection criteria using *detectsources* were as follows: a substamp image of 50x50 pixels used to estimate the flatfield background in a relatively 'empty' portion of the image; a 1.75σ threshold over the background RMS deviation; convolution of the input image with a 2D Gaussian kernel with full-width at

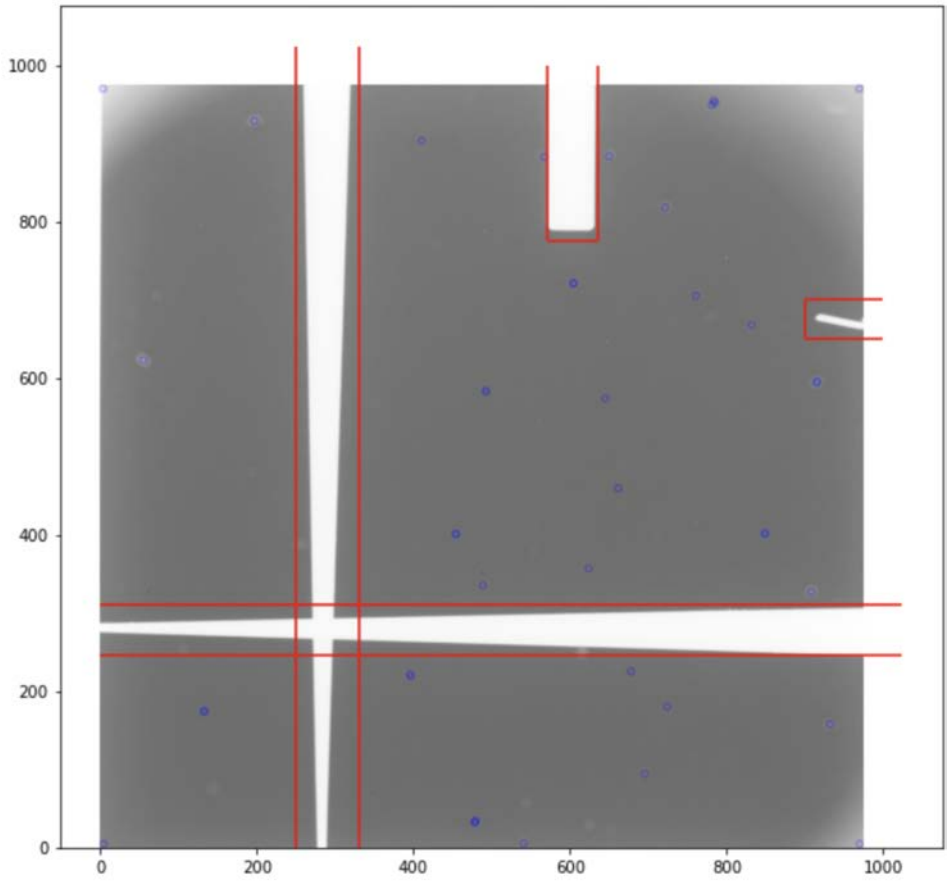

Figure 2. Example of the coronagraphic bar and wedge features in an inverted 50CORON flatfield. Coronagraphic occulter features were masked out (red box regions) for mote identification and extraction in a preliminary analysis using the DAOStarFinder algorithm. The full analysis presented in this report uses only the unocculted 50CCD flatfields for consistency.

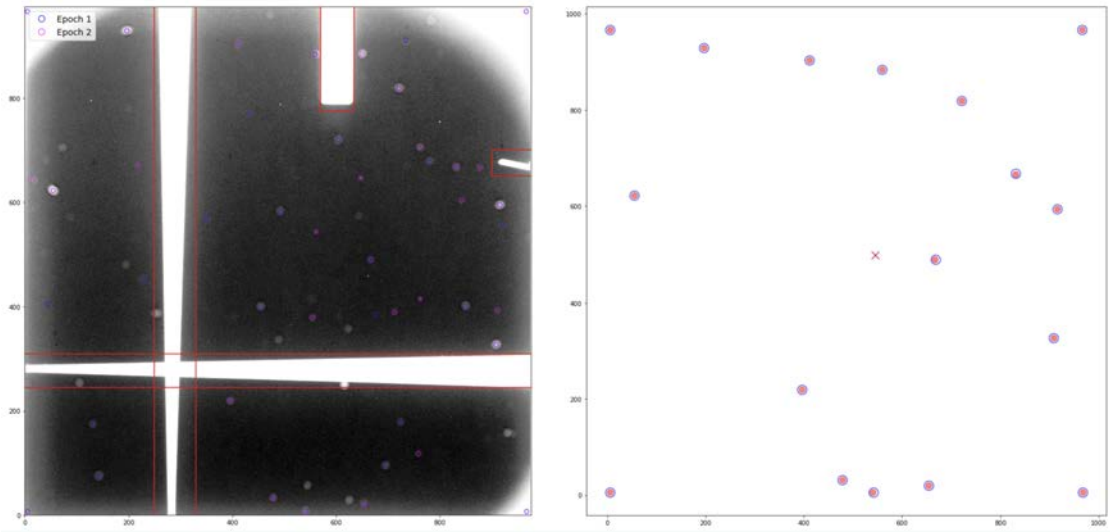

Figure 3. Example of a 50CORON flatfield (*left*) with source coordinates detected and matched across two epochs using the DAOStarFinder algorithm (*right*). The vignetting effects at the field corners are visible in the left inverted image. Blue circles correspond to the earlier epoch in time, while magenta (left) or red filled circles (right) correspond to the later second epoch, indicating mote motion.

half-maximum (FWHM) of 3 pixels, in order to smooth the noise and optimize mote detectability; and a 25 pixel "stellar" FWHM, given the out-of-focus nature of the dust motes and their relatively extended spatial properties. A visualization of a trimmed, inverted 50CCD flat and its corresponding dust mote source detections using *detectsources* is shown in Figure 4.

2.1.3 Mote catalog

In order to reliably identify the higher 'signal-to-noise' motes that are shared across all of the epochs, a catalog of 55 unique motes was generated by extracting sources from within the median image of all 69 individual 50CCD flatfields. We then compared this catalog against motes extracted from each of the individual epochs to determine which motes were identified in common across all flatfields.

2.2 Rotation measurement approaches

After generating a source catalog of all 55 dust mote x- and y-positions in each epoch, pairs of motes between the first epoch (used as a reference), and each subsequent epoch were matched. We did this by comparing both the x- and y-positions and finding pairs that matched within a 1.0 pixel threshold in each axis. This is a reasonable tolerance given the sparse nature of the motes in the flatfields and the expected positional

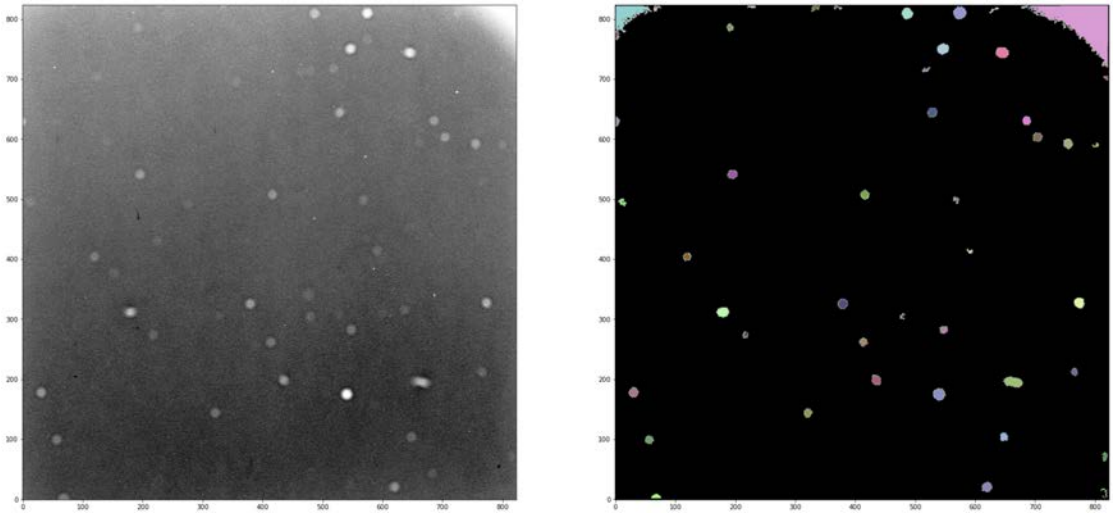

Figure 4. Example of the 50CCD flat (*left*) and mote extraction map (*right*) using the *detectsources* algorithm.

offset of only 0.3 pixels per decade of motion, as estimated from the spectral trace and astrometric approaches.

Within each epoch, the median position of all of the motes was calculated and assumed to be the center of rotation for that epoch. A vector for a given mote in each epoch was calculated relative to the epoch's center of rotation. We then calculated the angle between the reference epoch vector and the later epoch vector to determine the amount of rotation for a given mote relative to its position in the reference epoch.

2.2.1 Alternative center of rotation calculation

A bisector analysis was performed to measure the center of rotation in aggregate across all epochs (as opposed to simply using the median mote positions). In this approach, for a given dust mote, the slope and intercept of a connecting line between the mote's initial position and its final position was calculated, allowing for determination of the perpendicular bisector to that line. Then, for each pair of two dust motes in the field, the intersection of their perpendicular bisectors was assumed to be the center of rotation, and the median value of all 1485 possible pairs in each axis was taken to be the overall center of rotation.

3. Results

3.1 Mote identification across epochs

Motion between the earliest and latest epoch can be seen in the visual representation of a vector diagram in Figure 5, where the initial epoch position is shown with a larger open blue symbol, and the final epoch is shown with a smaller filled red circle. The vector of motion has been scaled up by a factor of 200× for visibility. While a large amount of scatter in mote motion is visible given uncertainties in centroiding the mote positions, a general trend of clockwise rotation can be observed in the vector field. The center of rotation is only slightly offset from the median position of the motes in each epoch.

3.2 Rotation vs. time plots

From the extraction and motion calculations presented in the previous sections, the amount of rotation as a function of increasing epoch from the initial Cycle 8 reference epoch can be visualized. Figures 6 and 7 show the typical motion in each of the x- and y-axes for a given dust mote as a function of time, which illustrates the noise inherent in determining mote position, but also show generally increasing trends in both axes.

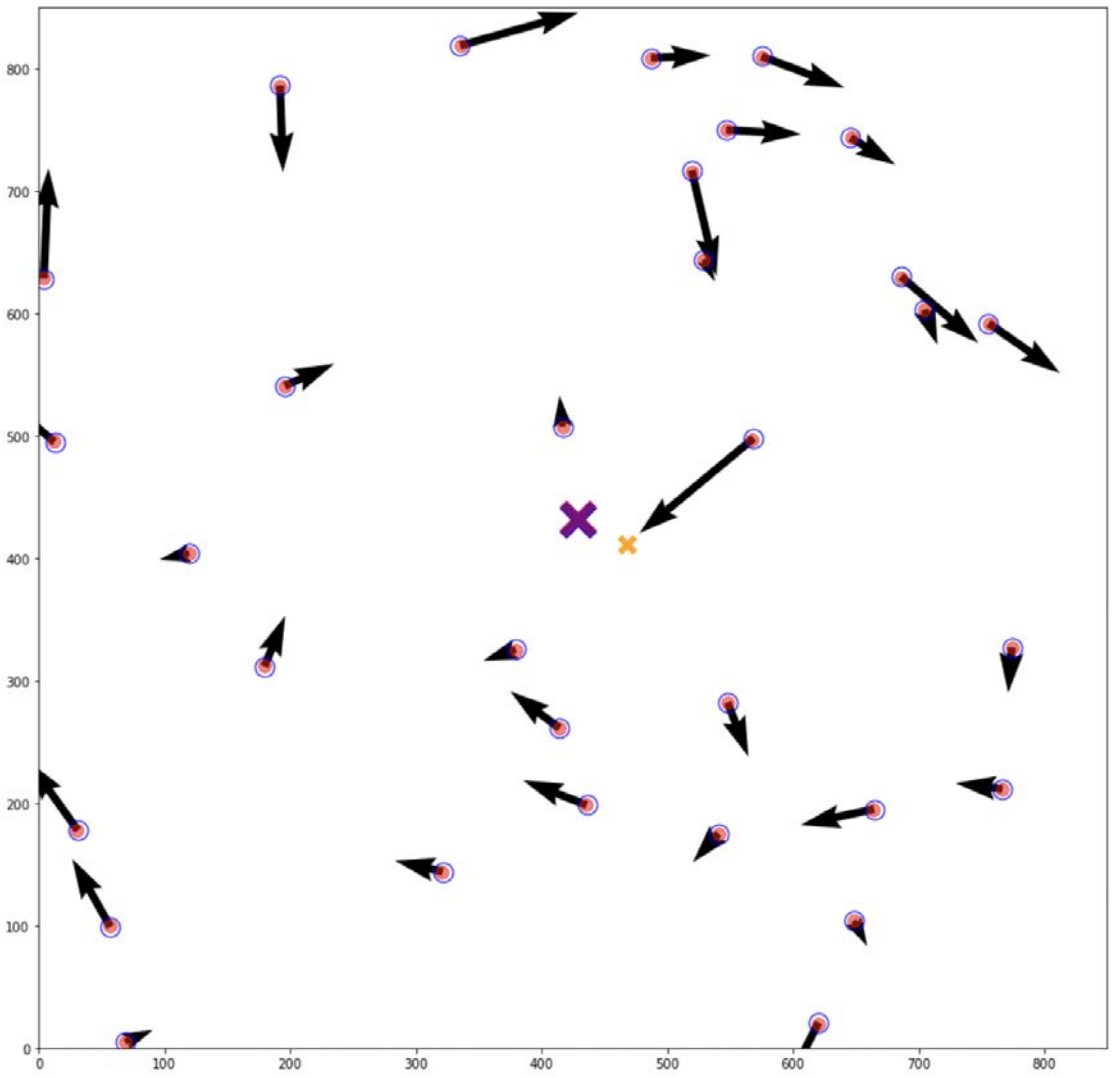

Figure 5. Vectors showing the motion between the first epoch (blue open circle) and final epoch (red filled circle), with the vector size scaled up by a factor of 200×. The median mote position between the first and final epochs is shown in reduced-opacity blue and red x-symbols, respectively, which overlap to the degree that they are nearly visible as a single purple x-symbol. The center of rotation derived from a bisector analysis between the first and final epochs is shown with the small orange x-symbol.

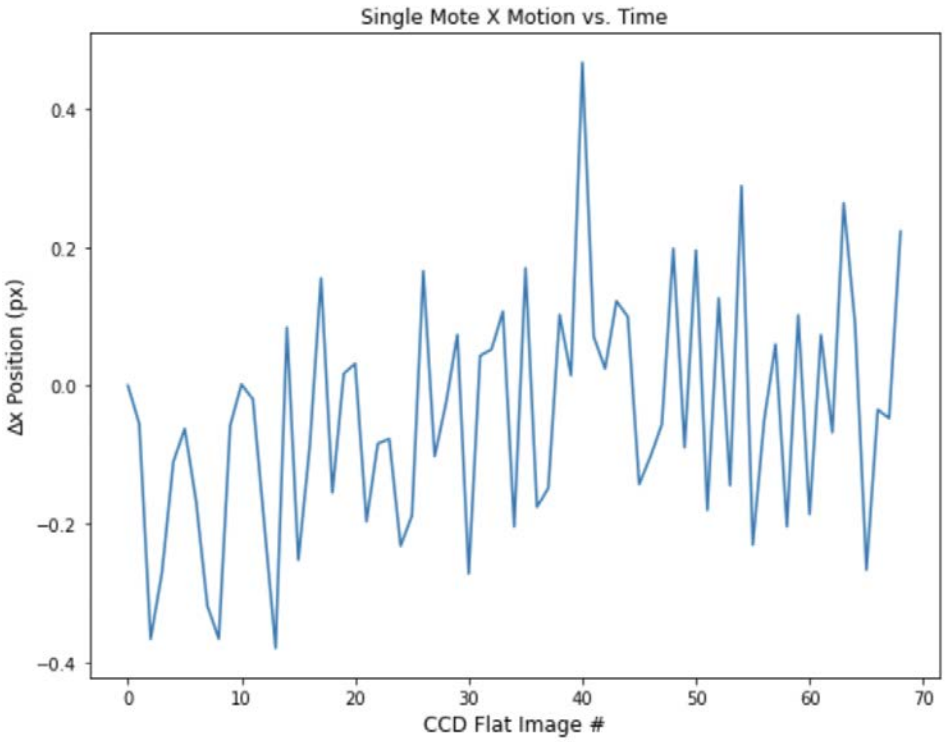

Figure 6. For an individual mote in the upper left quadrant of the image, the change in *x*-position relative to the reference epoch shown as a function of time (increasing flatfield image number).

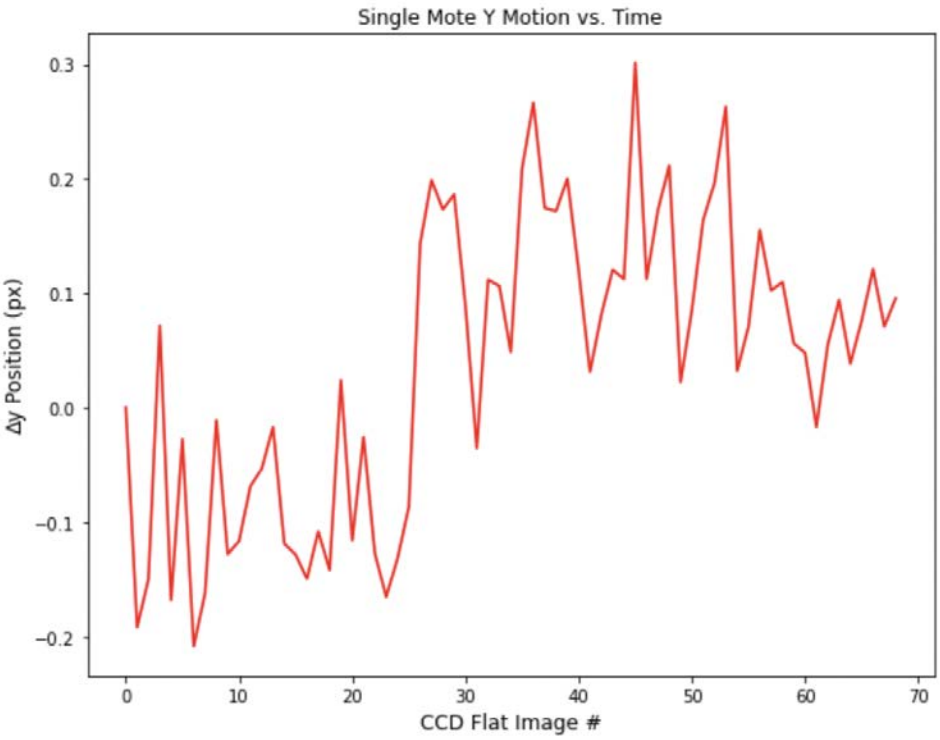

Figure 7. Same as Figure 6, but motion of the same individual mote in the *y*-axis over time.

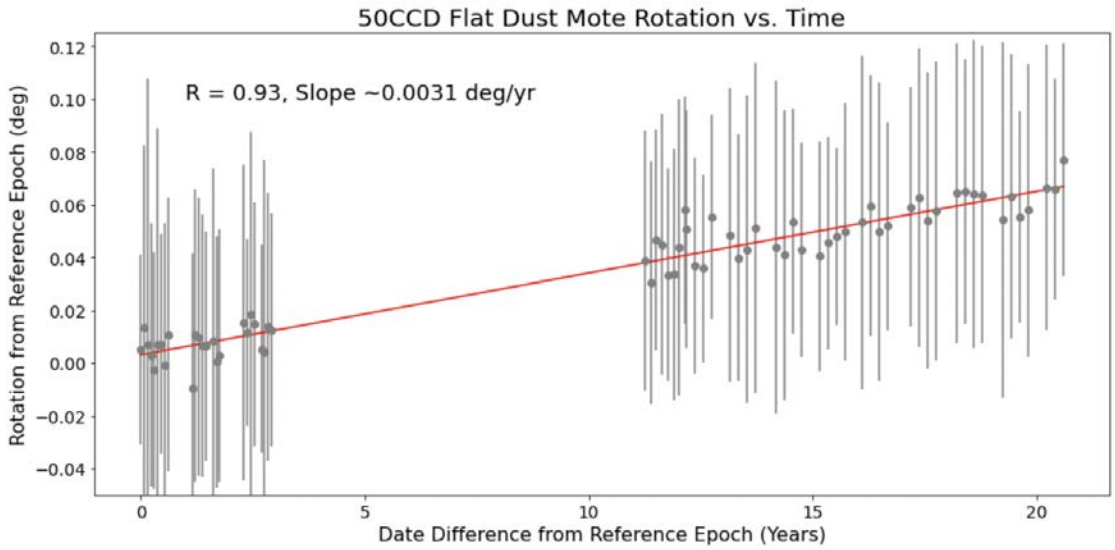

Figure 8. Results from extracting the dust mote positions from over 20 years of STIS 50CCD flatfields and comparing their positions to those from the first epoch in time (Cycle 8), demonstrating the rotational trend. The gap in time corresponds to when STIS was offline prior to SM4. The dust mote rotation shows a rate of change of 0.0031 degrees/year, comparable to both the *Gaia* astrometric effect from archival science imaging (0.0038 degrees/year) and the rotation of the spectral traces observed in STIS CCD spectroscopy (0.003 degrees/year).

By taking the median amount of rotation for all 55 motes in each epoch relative to the reference epoch, the amount of rotation can be visualized as a function of time, as shown in Figure 8. Despite the large scatter (calculated as the standard deviation of the 55 measurements per epoch), the increasing trend over the course of 20 years can be seen and a linear regression was performed to ascertain the value of the slope, which was calculated to be 0.0031 degrees/year.

Given the large uncertainties on any given epoch inherent in the mote extraction process, which are likely overestimated given the tight relationship of the increase in rotation, a Markov-Chain Monte Carlo (MCMC) approach was used to fit the slope and determine its uncertainty. The values shown in Figure 8 were determined using the *emcee* package (Foreman-Mackey et al., 2013), with priors on slope and intercept drawn from a initial linear least-squares fit to the data (slope of 0.003 $\pm$ 0.001 and intercept of 0.003 $\pm$ 0.011). The resulting maximum likelihood approach (using 1000 walkers and 100,000 steps, discarding the first 1000 steps as burn-in) are visualized in Figures 9 with distributions on slope, intercept and parameter f, the latter of which represents the fractional overestimation of the true variance (uncertainty) on the data points. The posterior distributions in Figure 9 thus provide an estimate of the uncertainty on the given parameters, given as 68% confidence intervals, with values of slope = 0.0031$\pm$0.0001, intercept of 0.00256$\pm$0.0001, and $\log(f)$ = 17.8379$\pm$0.0001.

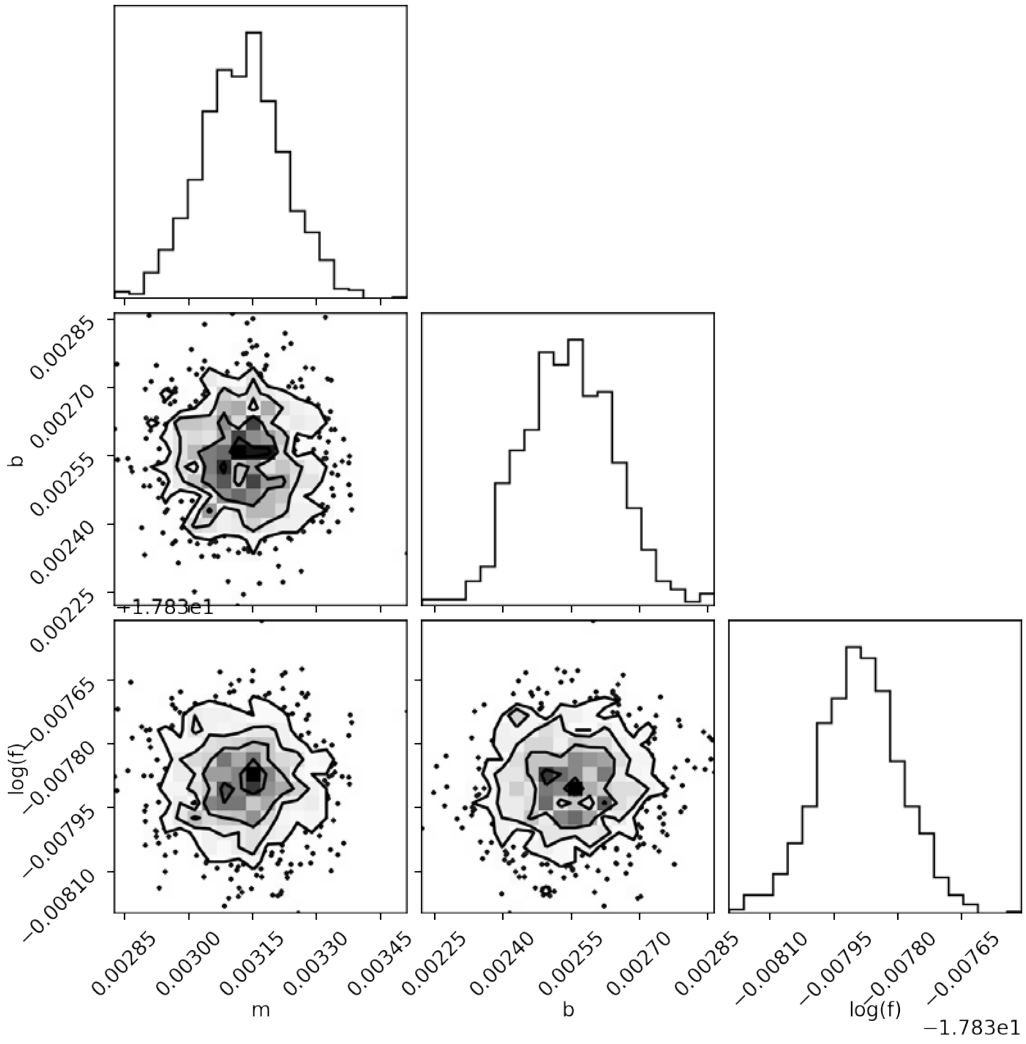

Figure 9. Posterior distributions on the slope (m), intercept (b), and fractional variance fit (f) using the *emcee* package to the rotation data shown in Figure 8.

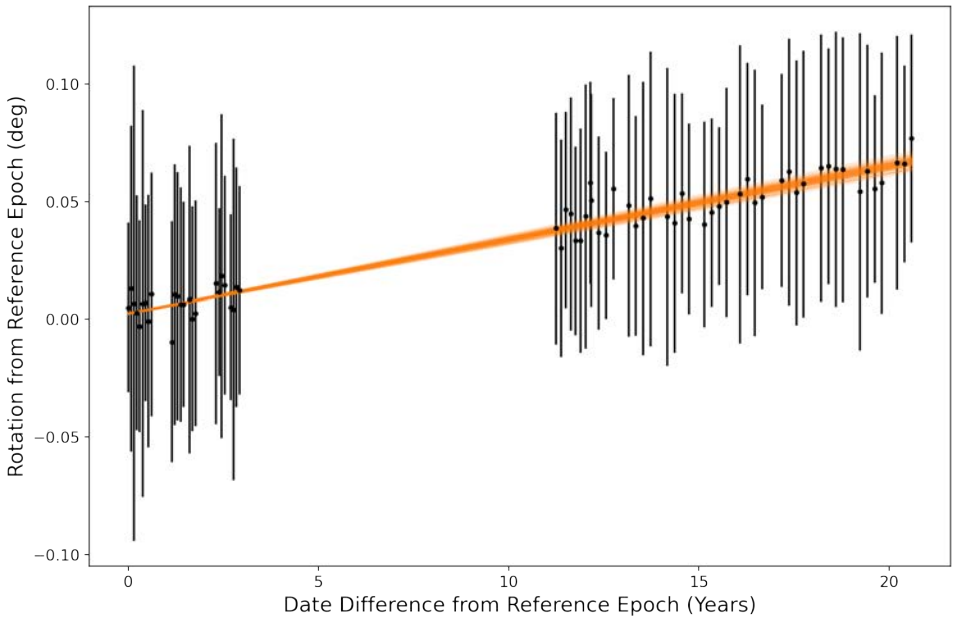

Figure 10. Distribution of 100 best-fit lines from the MCMC run shown in orange, overlaid on the data shown in Figure 8.

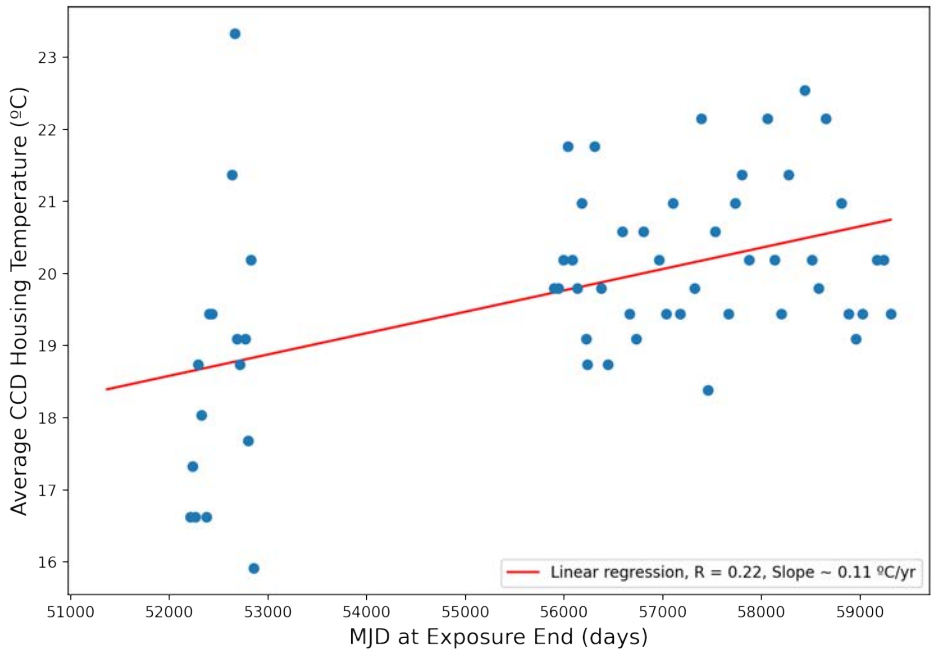

Figure 11. Average CCD housing temperature, extracted from the FITS headers of the 50CCD flatfields in this analysis, plotted as a function of time. The gap corresponds to the offline period of STIS prior to SM4. The very weak positive correlation of R=0.22, illustrated by the red model fit, disappears when fitting only the post SM4 data.

3.3 Environmental correlations

To understand if ambient environmental conditions of the CCD were correlated with the amount of observed rotation, the header keyword 'OCCDHTAV', corresponding to the average CCD housing temperature, was queried as a function of time from the flatfield headers. Figure 11 shows all non-negative header temperature values in degrees Celsius plotted as a function of the modified Julian date for the flatfields considered in this analysis. All flatfields prior to MJD 52000 stated a uniform CCD housing temperature, as prior to MJD 52000, STIS was operated with the primary Side-1 electronics and was maintained at an operating temperature of -1ºC. (When Side-1 failed, the change-over to Side-2 electronics in May 2001 also resulted in the loss of direct temperature control.) A linear regression was performed, showing a positive correlation with slope of $\sim$0.11ºC/year and a correlation coefficient of R=0.22, suggesting only a very weak correlation between the two quantities. Excluding the data from pre-SM4 and refitting resulted in virtually no correlation, with R=0.01 and a slope fit of 0.04ºC/year.

4. Conclusions and Recommendations

From an analysis of the motion of individual dust motes in STIS 50CCD flatfields taken over the course of 20 years between Cycles 8 and 28, we find evidence for a long-term, slowly-varying rotational drift of 0.0031 $\pm$ 0.0001 degrees per year. Based on comparison with previous studies using complementary datasets and analyses, this rotational effect appears to be intrinsic to the CCD alone within STIS, and may be a physical effect of mechanical origin.

4.1 Comparison with spectral trace rotation and Gaia astrometry

Comparing the method presented here to measure CCD rotation with the other two techniques described in Section 1, we find the following values:

Reference	Method	Slope (deg/yr)
(this work)	Dust mote rotation in flatfields	0.0031 $\pm$ 0.0001
Nguyen et al. (2021)	North angle astrometry with *Gaia* sources	0.0038
Dressel et al. (2007)	Spectral trace rotation - G230LB	0.0031 $\pm$ 0.0003
Dressel et al. (2007)	Spectral trace rotation - G430L	0.0041 $\pm$ 0.0001
Dressel et al. (2007)	Spectral trace rotation - G750L	0.0037 $\pm$ 0.0003

Table 1. Comparison of estimated CCD rotation slope values using three distinct techniques.

Note that there exists disagreement at the $\geq 3\sigma$ level for some of these estimates, even within a given technique. For the comparison with *Gaia* astrometry in a given epoch of data examined in 2017, Nguyen et al. (2021) found an uncertainty on the average difference between the ORIENTAT keyword and true north angle of 0.002 degrees, so it may be reasonable to assume that this uncertainty could represent the measurement uncertainty in any given epoch. We note that 0.002 degrees is also similar in magnitude to the y-axis intercept of 0.00255 degrees fit in the dust mote rotation analysis in Section 3. If the rotational measurements in Table 1 share the same physical origin, then it may be valid to take the weighted average of the five measurements to determine an overall slope from the three different techniques of 0.00358 $\pm$ 0.00006 degrees/year (conservatively adopting 0.002 as the uncertainty on the *Gaia*-derived astrometric slope).

4.2 Offset to apply to ORIENTAT header keyword as function of time

Potential implementations of a correction to the rotation angle in the FITS header could be undertaken in a variety of ways. Based solely upon the flatfield rotational

analysis presented in this report, a correction to the existing orientation keyword can be calculated as follows: In order to determine the true north position angle of the y-axis of the detector (PA_y), a manual correction to the value in the ORIENTAT keyword based upon flatfield rotation can be applied using the following relationship:

$$PA_y \text{ (deg)} = 0.0031 \times [(\text{MJD} - 51369.5381426)/365.25] + 0.00255 + \text{ORIENTAT}$$

Where MJD represents the Modified Julian Date of the observation to be corrected, and the date of 51369.5381426 represents the first epoch of 50CCD flatfields considered in this analysis from Cycle 8 (1997-07-10). Note that this slope value is lower than that derived from astrophysical source astrometry from Nguyen et al. (2021) in Figure 1, and also lower than the G430L spectral trace from Dressel et al. (2007), although more comparable to the measurements of the G230LB and G730L traces. Therefore, an alternative estimate adopting the weighted average of the slopes using all three different techniques would be:

$$PA_y \text{ (deg)} = 0.00358 \times [(\text{MJD} - 51369.5381426)/365.25] + 0.00255 + \text{ORIENTAT}$$

with an assumption of $\pm$0.002 deg uncertainty on the final position angle.

As of writing, a correction for this offset has not been applied to existing STIS data. A number of implementations could be considered: the STIS science instrument aperture file (SIAF) could be updated such that the keyword is populated automatically; a reference file could be created to modify CALSTIS such that a correction for the offset is applied in the pipeline calibration itself (similar to the CCD reference files of spectral trace tables used for spectroscopy); and these could be updated accordingly in the *HST* calibration reference data system (CRDS). In the interim, for the purposes of scientific analyses requiring precision astrometry, the suggested approach is to calculate the appropriate position angle in degrees for a given epoch of observations using one of the relations provided above.

4.3 Next steps and potential physical origin

While identifying the exact physical mechanism responsible for the CCD rotational drift is outside the scope of this report, a more detailed investigation into the environmental conditions of the CCD may illuminate potential sources of the drift. We note that the change in the rotation angle is slow and secular, and a variety of mechanical explanations may be possible. For example, the behavior may be suggestive of a component under tension that has been gradually loosening since the instrument's original installation. For some ground-based spectrographs, outgassing has been attributed to slow shifts in echelle blaze angle (T. Gull, priv. communication). Other instrumental changes can lead to long-term variations, such as the switch from the primary Side 1 to secondary Side 2 electronics in May 2001, which led to some loss of thermal control and thus variable detector temperature dependent upon

spacecraft environmental conditions (Brown, 2001, ISR 2001-03). However, the rotational trend measured from the flatfields in this report and shown in Figure 8 precedes both the switch to Side 2 electronics and SM4, suggesting that the slow drift reported here may have a distinct, older origin.

Acknowledgements

We thank Ted Gull, members of the *HST* Mission Office, and Sarah Logsdon for helpful discussions on potential origins of the rotational effect, and suggested routes of investigation using various STIS diagnostics.

Change History for STIS ISR 2022-01

Version 1: 18 March 2022- Original Document

References

Astropy Collaboration, Price-Whelan, A. M., Sipőcz, B. M., et al. 2018, AJ, 156, 123

Brown, T. M. 2001, Temperature Dependence of the STIS CCD Dark Rate During Side-2 Operations, Space Telescope STIS Instrument Science Report (2001-03)

Dressel, L., Bohlin, R., Lindler, D., & Holfeltz, S. 2007, Time Dependent Trace Angles for the STIS First Order Modes, Space Telescope STIS Instrument Science Report (2007-03)

Foreman-Mackey, D., Hogg, D. W., Lang, D., & Goodman, J. 2013, PASP, 125, 306

Nguyen, M. M., De Rosa, R. J., & Kalas, P. 2021, AJ, 161, 22